



Performance of solid oxide fuel cells operated with coal syngas provided directly from a gasification process

Gregory A. Hackett^{a,b}, Kirk Gerdes^{a,*}, Xueyan Song^{a,c}, Yun Chen^{a,c}, Vaithiyalingam Shutthanandan^d, Mark Engelhard^d, Zihua Zhu^d, Suntharampillai Thevuthasan^d, Randall Gemmen^a

^aNational Energy Technology Laboratory, 3610 Collins Ferry Road, Morgantown, WV 26507, USA

^bOak Ridge Institute for Science and Education, 1299 Bethel Valley Road, Oak Ridge, TN 37830, USA

^cDepartment of Mechanical & Aerospace Engineering, West Virginia University, ESB Room G-70, Evansdale Drive, Morgantown, WV 26506, USA

^dEnvironmental Molecular Sciences Laboratory at Pacific Northwest National Laboratory, 902 Battelle Road, Richland, WA 99354, USA

H I G H L I G H T S

- ▶ First long-term exposure (500 h) of SOFC to direct syngas from a gasifier.
- ▶ Field application of mobile multi-cell array, capable of testing 12 cells at once.
- ▶ Sophisticated microscopy techniques used to investigate cell performance losses.

A R T I C L E I N F O

Article history:

Received 30 January 2012

Received in revised form

19 April 2012

Accepted 20 April 2012

Available online 3 May 2012

Keywords:

Solid oxide fuel cell

Coal syngas

Gasification

Multi-cell array

Transmission electron microscopy

Particle induced X-ray emission

A B S T R A C T

Solid oxide fuel cells (SOFCs) are being developed for integrated gasification power plants that generate electricity from coal at 50+% efficiency. The interaction of trace metals in coal syngas with Ni-based SOFC anodes is being investigated through thermodynamic analyses and in laboratory experiments, but test data from direct coal syngas exposure are sparsely available. This effort evaluates the significance of performance losses associated with exposure to direct coal syngas. Specimen are operated in a unique mobile test skid that is deployed to the research gasifier at NCCC in Wilsonville, AL. The test skid interfaces with a gasifier slipstream to deliver hot syngas to a parallel array of twelve SOFCs. During the 500 h test period, all twelve cells are monitored for performance at four current densities. Degradation is attributed to syngas exposure and trace material attack on the anode structure that is accelerated at increasing current densities. Cells that are operated at 0 and 125 mA cm⁻² degrade at 9.1 and 10.7% per 1000 h, respectively, while cells operated at 250 and 375 mA cm⁻² degrade at 18.9 and 16.2% per 1000 h, respectively. Spectroscopic analysis of the anodes showed carbon, sulfur, and phosphorus deposits; no secondary Ni-metal phases were found.

Published by Elsevier B.V.

1. Introduction

Solid oxide fuel cells (SOFCs) designed for operation on synthesis gas (syngas) derived from coal must be resistant to deleterious reactions between the Ni-based anodes and trace metals in the gas feed stream. At the elevated temperatures of conventional SOFC operation, many Ni-metal phases can form that impact the anode physical and electrocatalytic properties, as well as the microstructure. The thermodynamic potential for reaction between trace metals in coal-derived syngas and nickel in the

anode has been investigated [1–3]. Antimony, arsenic, cadmium, chlorine, lead, mercury, phosphorus, selenium, and sulfur are thermodynamically predicted to be present in coal-derived syngas that is cleaned at temperatures >300 °C. The mechanisms by which elements interact with the Ni-based anode can be distinguished and separated into three classes relating observable, time-dependent performance decreases in cell potential (or current density) with specific physical processes [4]. Class I degradation is typified by interactions in which physical obstruction of the gas diffusion path in the anode pores occurs from deposition of dense foreign material such as silicates or coke. Class II degradation occurs when species are selectively adsorbed onto active surface sites within the anode and block the access of principal fuel molecules (H₂ and CO). Class III degradation results from solid state reactions between trace metals and the anode nickel, which produce either

* Corresponding author. Tel.: +1 304 285 4342.

E-mail addresses: Gregory.Hackett@netl.doe.gov (G.A. Hackett), Kirk.Gerdes@netl.doe.gov (K. Gerdes).

Nomenclature

c-YSZ	Cubic Yttria Stabilized Zirconia	Ni/YSZ	Nickel/Yttria Stabilized Zirconia
DOE	Department of Energy	OCV	Open Circuit Voltage
EMSL	Environmental Molecular Science Laboratory	PIXE	Particle Induced X-Ray Emission
FC	Fuel Cell	PNNL	Pacific Northwest National Laboratory
FTIR	Fourier Transform Infrared Spectroscopy	PRB	Powder River Basin
HRTEM	High Resolution Transmission Electron Microscopy	PSDF	Power Systems Development Facility
ICP/MS	Inductively Coupled Plasma/Mass Spectroscopy	SCU	Syngas Cleanup Unit
IGFC	Integrated Gasification/Fuel Cell	SEM	Scanning Electron Microscope
LSM	Lanthanum–Strontium–Manganate	SOFC	Solid Oxide Fuel Cell
MCA	Multi-Cell Array	TEM	Transmission Electron Microscope
NCCC	National Carbon Capture Center	ToF-SIMS	Time-of-Flight Secondary Ion Mass Spectroscopy
NETL	National Energy Technology Laboratory	t-YSZ	Tetragonal Yttria Stabilized Zirconia
		XPS	X-ray Photoelectron Spectroscopy

solid solutions or distinct secondary phases. Typically the resulting solutions or secondary phases will possess properties less suitable for SOFC operation than the originally engineered phases.

To control integrated gasification/SOFC (IGFC) system costs, it is necessary to optimize the cleanup process for trace material removal. Trace material content in the syngas must be suppressed to a level that results in acceptable cell degradation rates without raising system cost to a prohibitive level. Experiments conducted for individual contaminant exposures are necessary to fully evaluate the physical nature of independent trace material interactions, and facilitate correlation of the degradation classes noted above with performance degradation observable in the cell output. Independent laboratory experiments have examined anode degradation for various trace material exposure thresholds, and published reports demonstrate degradation associated with exposure to elements including arsenic (As, [5–11]), cadmium (Cd, [11]), chlorine (Cl, [7–13]), mercury (Hg, [8–11]), phosphorus (P, [5,7–11,14,15]), lead (Pb, [11]), antimony (Sb, [11,16]), and selenium (Se, [17]). The required magnitude of trace metal removal has also been the subject of recent investigations [12,18–22].

The results of both thermodynamic and experimental investigations emphasize the critical requirement for adequate trace metal removal from syngas delivered to SOFCs. Cleanup targets have been proposed that are based on theoretical calculations derived from data on individual contaminant exposure in a laboratory environment [4], but no experimental information is presently available from tests conducted by exposing the SOFC to direct coal syngas in a representative industrial environment. Exposure of the SOFC to the more complex gas matrix present in the industrial process will facilitate examination of synergistic degradation that may occur when the anode is subjected to multiple trace materials simultaneously. By analyzing the cell performance degradation under such conditions, the adequacy of current theoretical and laboratory tests in predicting cleanup thresholds may be evaluated.

In this work, SOFC specimen are exposed to direct syngas derived from coal gasification to investigate the impact on cell performance. Post-operational spectroscopic investigation of cell anodes is conducted using SEM, TEM, ToF-SIMS, PIXE, and XPS in an effort to correlate the observed performance degradation directly with changes in the anode phases or structure. In particular, the operated cells are thoroughly examined for silicon and carbon deposits and for evidence of the formation of nickel-metal secondary phases.

2. Experimental

Direct syngas exposure testing of fuel cell (FC) specimen was conducted in conjunction with operation of the research transport gasifier at the National Carbon Capture Center (NCCC) at the Power

System Development Facility (PSDF) in Wilsonville, AL. The NCCC/PSDF is a state-of-the-art facility sponsored by the U.S. Department of Energy (DOE) as a test center dedicated to the evaluation and provenance of clean coal technology. At the time of testing, the facility featured a 50 lb min⁻¹ syngas slipstream (now 500 lb min⁻¹) which is available to outside developers and researchers to support evaluation of innovative gasification process technology on a pilot scale. The slipstream flows to a host-operated Syngas Cleanup Unit (SCU), which is a configurable cleanup train that facilitates tailoring of the syngas composition according to user requirements.

Details of the NCCC/PSDF gasifier and operation are available in other reference documents [23], and a simplified process flow schematic is shown in Fig. 1 ref. [24]. Syngas fuel was provided by gasification of Powder River Basin (PRB) coal. After gasification, the syngas was filtered in a high temperature candle filter at 500 °C and then fed to the SCU for sulfur removal using a sulfur sorbent operating at a temperature of approximately 500 °C. The syngas was then made available via header pipeline maintained at 250 °C and 160–190 psig.

The syngas composition was analyzed daily for bulk composition and hydrocarbon presence (via FTIR) and periodically for trace species (via traditional liquid digestion ICP/MS and a directly coupled GC-ICP/MS system) and sulfur content. Additional fuel flow (H₂ and N₂) and oxidant flow (air) data were collected as well as fuel feed pressure data, and cell and operation temperature data.

In order to increase the total amount of test data available, fuel cell test specimens are operated on syngas fuel using a parallel array of 12 button cells known as the Multi-Cell Array (MCA). The MCA is integrated into a mobile SOFC test apparatus capable of interfacing with industrial gas supply sources and processes. The fuel gas is distributed evenly to each individual cell using a common fuel supply manifold, and cells are simultaneously exposed to air in a common oxidant reservoir. The applied electrical load to each cell can be controlled independently. All cells are commonly heated in a furnace operated at 800 °C and 1 atm. The fuel cell specimen tested are anode supported cells consisting of a 750 μm Ni/YSZ anode, a 10 μm YSZ electrolyte, and an 80 μm LSM cathode. The cells are approximately 2.9 cm in diameter with a 2 cm² active area.

SOFC specimen were prepared to receive syngas from the SCU by following a standardized pre-conditioning routine. Cells were heated in air (cathode side) and nitrogen (anode side) from ambient conditions to 850 °C at 2 °C min⁻¹. The furnace temperature dwells at 850 °C for 30 min (to ensure proper wetting of the glass seal system) before decreasing to 800 °C at 2 °C min⁻¹, where the temperature dwells for the duration of the test. Cells are then fed with H₂/N₂ mixtures, with the H₂ content increasing incrementally over several hours until the fuel composition is 100% H₂. Cells are then operated for approximately 24 h at a current density of 250 mA cm⁻² to prepare them uniformly for exposure to the syngas.

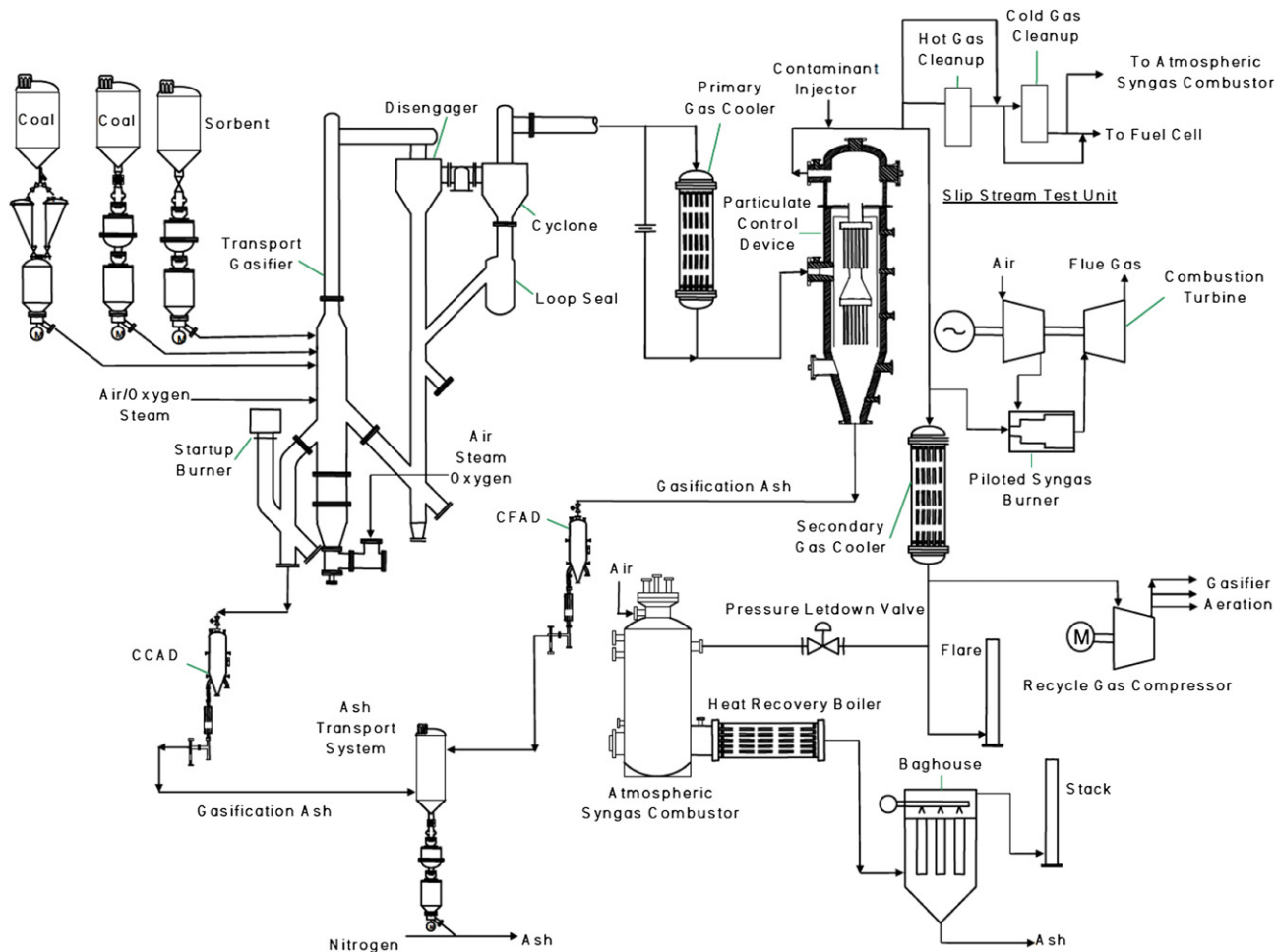


Fig. 1. Flow diagram of the PSDF gasifier train [24].

Under pure H_2 fuel at this current density, cells uniformly demonstrated open circuit potentials of 1.217 ± 0.015 V and power densities in the range of $200\text{--}225$ $mW\ cm^{-2}$ @ $0.8\text{--}0.9$ V, which is typical of this cell construction and gas condition. After 24 h of operation on H_2 , the load was removed and fuel feed was switched to direct syngas. Syngas was initially introduced to each cell at an approximate rate of 180 sccm, and enriched with approximately 9 sccm of pure H_2 to increase the operating performance. Load was re-applied to each cell at different magnitudes (0 $mA\ cm^{-2}$, 125 $mA\ cm^{-2}$, 250 $mA\ cm^{-2}$, and 375 $mA\ cm^{-2}$) to allow investigation of the impact of cell load on performance degradation. During the course of operation cell voltage was monitored to ensure that the potential remained above 0.6 V. Current densities were adjusted down for cells that degraded below 0.6 V as needed.

Cell operation was monitored for approximately 500 h at these operating conditions. At the completion of the test, the cells were uniformly cooled to ambient conditions under air (cathode) and nitrogen (anode) at $2^\circ C\ min^{-1}$. The apparatus was deconstructed and the cells prepared for post-trial analysis. The results are reported in the following section.

3. Results and discussion

3.1. Benchmark performance

When performing experiments through a direct interface to an industrial process, care must be taken to analyze data in the context

of near-constant fluctuation of process operating conditions. In the present case, performance comparisons obtained in the industrial setting require comparison to a benchmark test obtained in a laboratory environment. The comparison enhances the distinction between the three primary sources of systematic variability present in these tests: 1) the normal distribution of cell performance for a given batch of commercial cells; 2) the normal position to position variability inherent in the MCA apparatus; and 3) the daily variations in plant process conditions affecting gas quality and delivery.

Systematic variability associated with the expected performance of the as-received cell specimen and variability inherent to the position of the cell within the MCA apparatus are addressed in controlled laboratory tests. Five rounds of tests are conducted with a full array of 12 cells using materials obtained in the same commercial batch as cells installed for the direct syngas testing. The cells are standard anode supported button cells featuring an LSM cathode, assembled in the MCA in the same manner as previously described. Cells are treated according to identical thermal, gas conditioning, and operating conditions, except that current density is maintained at a constant value of 250 $mA\ cm^{-2}$ for all cells throughout the test.

Data and statistical analysis for the baseline cell performance test are shown in Table 1. Of the possible 60 test cells, 43 produced normal operating performance (72%). Results are considered normal if the average cell voltage for cells tested in a given location is within three standard deviations of the net average cell voltage of all cells tested under identical conditions. The data show that the average expected performance from each cell is in a narrow band of

0.857 ± 0.008 V under 250 mA cm^{-2} load and 1.132 ± 0.012 V at open circuit conditions with a standard deviation of 26 mV and 44 mV, respectively (range based on 95% confidence). Data and statistical analysis from the five completed baseline tests show less than 2% variability from position to position, and no statistically significant distinction can be made from operation of cells in one position or another. These results are also used to qualify data obtained in the direct syngas test, where the risk of in-situ cell failure is somewhat greater than in the more controlled laboratory environment.

3.2. Fuel characterization

The evaluation of sources of systematic variability in the plant process conditions is extremely complex. In order to simplify an assessment, and to focus on the primary factor of relevance to the present effort, fluctuations in the daily fuel gas composition are assessed. Fluctuations in gas composition primarily impact the cell by altering the Nernst potential, which provides a theoretical electrochemical operating condition. Fig. 2 shows a daily evaluation of bulk gas composition and the calculated Nernst potential. The bulk syngas composition on a dry-basis was typically 15% H_2 , 5% CO , 1% CH_4 , 65% N_2 , and 13% CO_2 in air blown mode (first 375 h of cell operation). Water was present at approximately 7%. In oxygen blown mode (final 75 h of cell operation), the dry-basis gas composition was 22% H_2 , 5% CO , 1% CH_4 , 60% N_2 , and 12% CO_2 , while water content increased to approximately 10%. Obvious daily changes are observable through the entire run duration, especially in Days 9–12 (approximately 2 to 300 h). On these days the fuel stream water content increased, and Nernst potential was depressed by up to 25 mV. Fuel gas composition in Days 16–20 is also shown to produce a relatively depressed Nernst potential. During this period, the gasifier switched from an air-blown operation to oxygen-blown operation, which increases the syngas water content. The Nernst potential varies from a low of 0.907 V to a high of 0.948 V. The average Nernst potential is 0.932 ± 0.006 V.

After filtering and sulfur removal treatments, the syngas contained trace materials including sulfur (<2 ppm) and ammonia (1700 ppm). The hydrocarbon content of the fuel gas stream was also monitored regularly. Fig. 3 depicts the daily concentration of the principal higher order hydrocarbons such as ethylene, benzene, and naphthalene. The concentration of hydrocarbon material is seen to fluctuate daily, and hydrocarbon concentration depression is evident in Days 9–12, where the steam content is elevated.

The trace metal content of the syngas was analyzed using methods based on ICP/MS. Traditional liquid ICP/MS analysis provided by PSDF detected Hg, Cr, Pb, Ni, Se, Sn, and Zn in the syngas over two days of analysis, and a summary of the measured trace material concentrations are shown in Table 2. A prototype GC-ICP/MS system was also deployed to support analysis, and the

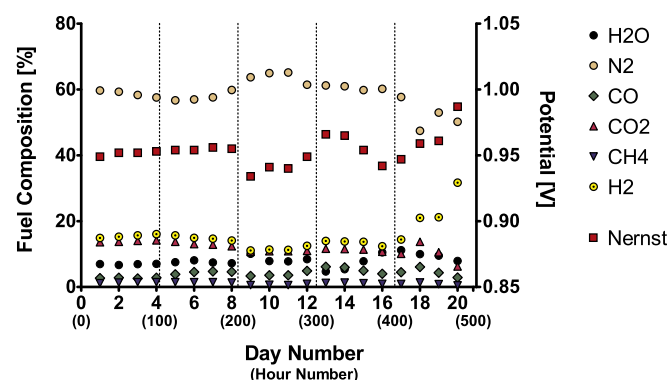


Fig. 2. Daily fuel composition and calculated Nernst potential.

device confirmed the presence of Hg, Cd, Zn, and Cr, but the concentrations could not be quantified. According to both testing methods As, Ge, and Sb were not present above the instrumental limit of detection, which is estimated to be better than $10 \mu\text{g m}^{-3}$ for these elements.

3.3. Electrochemical operation

The validity of the output data must be evaluated to provide confidence in the analysis of the cell performance. Evaluation distinguishes the source of cell performance degradation, whether due to operating conditions or failure in a portion of the testing apparatus. Test apparatus or specimen failures may include fuel/oxidant leakage due to improper sealing around the cell, poor mechanical contact of the current collecting meshes with the cell surface or transfer wires, or mechanical cell failures (cracking, delamination, etc). Such failure modes can be diagnosed through examination of the electrochemical data and post-trial analysis. A summary of the electrochemical data is provided in Table 3 and Fig. 4.

According to Table 3 and Fig. 4, the relatively high overpotential associated with cells 7, 8, and 12 immediately identify them visually as potential outliers. A non-linear analysis shows an upper 95% confidence interval (dashed line) that does not include these three cells, which is further indication that these cells are outliers. The coefficient of determination, R^2 , of the regression for the remaining nine cells is 0.828, improved from 0.048 when all 12 are included. This analysis is conducted by GraphPad Prism software which uses the False Discovery Rate method to determine regression outliers [25]. The designation of these values as outliers is further corroborated by Cook's Distance Measurement method which analyzes the residuals of each data point for their influence on the regression curve.

These cells are well beyond the established operating trend and its corresponding error; therefore, it can be concluded that these results were obtained for test apparatus or specimen failure and degradation results are not attributable to operating conditions such as fuel composition or electrochemical load.

Next, the degradation in the individual cell performance over time is evaluated to identify degradation occurring beyond that associated with the baseline cell. Baseline cell degradation is often attributable to microstructural failures due to thermal decomposition of the cell structure [26,27]. This type of degradation is expected to be slow and on the order of <1% per 1000 h [28]. Degradation rates that are statistically greater may be attributable to modes associated with the fuel source according to any of the three broad classes of degradation. Additional analysis including post-trial spectroscopy is required to assign the observed degradation to a specific mode.

Table 1
Summary of MCA repeatability testing.

Samples	43	
Current density	0.25	A cm
Average potential	0.857	V
Average potential STD	0.026	V
Coefficient of variation	3.0%	
95% Confidence interval	± 0.008	V
99% Confidence interval	± 0.010	V
Average OCV	1.132	V
Average OCV STD	0.044	V
Coefficient of variation	3.9%	
95% Confidence interval	± 0.012	V
99% Confidence interval	± 0.015	V
Average overpotential	0.275	V

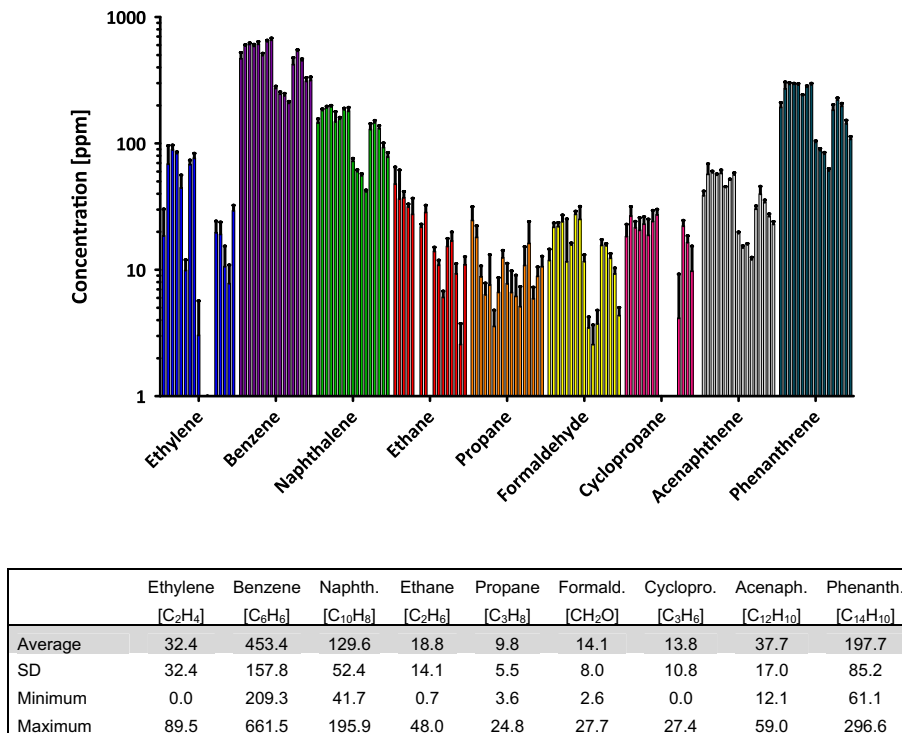


Fig. 3. Daily plot of each monitored hydrocarbon and tabulated summary of data [in ppm]

Over the 450 h operating period, cell loadings were fixed at four levels, and cells were adjusted according to their performance. Results of the temporal cell potential are displayed in Figs. 5–8. The figures each contain data for the cells operated at a given current density, and show the relative and absolute times of operation for a given cell. Fig. 5 depicts the cell potential at 0 mA cm⁻² (cells 1, 4, 5, and 11), Fig. 6 depicts cell potential at 125 mA cm⁻² (cells 2, 3, 9, and 10), Fig. 7 depicts cell potential at 250 mA cm⁻² (cells 2, 5, 6, and 9), and Fig. 8 depicts cell potential at 375 mA cm⁻² (cells 1, 4, and 10). In all four figures the plots labeled ‘A’ depict the potential data for all cells operating at a given current density while the plots labeled ‘B’ depict the deconvoluted cell data. Cell performances are characterized by applying a non-linear regression to data obtained at specific current density. Data obtained from relatively short duration operation (<100 h) at a given current density yield anomalous results, especially near the start of operations. These data show anomalous increases in performance due to their short operating duration, and may not be reliable. Degradation rates for all cells are generated on the basis of continuous operation at a given current density for more than 100 h, and current density specific degradation rates are estimated by including all data for cells operated at a given current density for more than 100 h. The degradation rates at each current density are shown in Table 4.

3.4. Post-trial analysis

The cells tested for 450 h on direct syngas were post-operationally analyzed at the Environmental Molecular Science

Laboratory (EMSL) facility at the Pacific Northwest National Laboratory (PNNL). The cells were subjected to X-ray Photoelectron Spectroscopy (XPS), Time-of-Flight Secondary Ion Mass Spectroscopy (ToF-SIMS), and Particle Induced X-ray Emission (PIXE). Cells were also examined by TEM using facilities and equipment at West Virginia University, and by SEM at NETL.

3.4.1. XPS

XPS measurements were performed using a Physical Electronics Quantum 2000 Scanning Electron Spectroscopy for Chemical Analysis (ESCA) Microprobe. This system uses a focused monochromatic Al K α X-ray source (1486.7 eV) and a spherical section analyzer. The instrument has a 16 element multichannel detector. The X-ray beam used was a 100 W, 100 μ m diameter beam that was rastered over a 1.3 mm \times 0.2 mm rectangular sample. The X-ray beam is incident normal to the sample and the photoelectron detector was at 45° off-normal. Wide scan data were collected using a pass energy of 117.4 eV.

XPS is useful in analyzing the surface chemistry (1–10 nm depth) of a sample. The complete results are given below (in atomic %) in Table 5.

A substantial amount of carbon is located on the surface, much higher than the natural background contamination levels. This is likely deposited from hydrocarbon decomposition reactions, which will lead to either Class I or Class III degradation. Also of note is the indication of the presence of P, which is known to create secondary phases with nickel from the anode. However, there were no Ni_xP_y secondary phases found in any of the analyzed samples. Also located were Al, La, Ni, and Si.

Table 2
Summary of trace element composition of the direct coal syngas [in ppm].

Sample	Antimony [Sb]	Arsenic [As]	Cadmium [Cd]	Chromium [Cr]	Germanium [Ge]	Lead [Pb]	Mercury [Hg]	Nickel [Ni]	Selenium [Se]	Sulfur [S]	Tin [Sn]	Zinc [Zn]
1	<DL	<DL	<DL	3.5	<DL	1	2.1	2.3	0.9	<2	42.6	53.4
2	<DL	<DL	<DL	2.7	<DL	3.2	9.4	2.1	0.8	<2	179.5	94.6

Table 3
Summary of cell potential data.

Cell	Nominal setpoint [A/cm ²]	Average current density [A/cm ²]	Average potential [V]	Standard deviation	95% confidence interval [V]	Average Nernst potential [V]	Average overpotential [V]
1	0.000	0.056	0.926	0.194	±0.002	0.954	0.028
2	0.250	0.201	0.717	0.177	±0.002	0.954	0.238
3	0.125	0.121	0.810	0.157	±0.002	0.954	0.144
4	0.375	0.311	0.667	0.177	±0.002	0.954	0.287
5	0.250	0.143	0.747	0.273	±0.003	0.954	0.207
6	0.250	0.137	0.726	0.297	±0.003	0.954	0.228
7	0.125	0.068	0.579	0.251	±0.002	0.954	0.375
8	0.000	0.042	0.510	0.253	±0.003	0.954	0.444
9	0.125	0.132	0.817	0.195	±0.002	0.954	0.137
10	0.375	0.313	0.661	0.172	±0.002	0.954	0.293
11	0.000	0.008	0.951	0.177	±0.002	0.954	0.003
12	Varies	0.110	0.530	0.200	±0.002	0.954	0.424

3.4.2. ToF-SIMS

Time-of-Flight Secondary Ion Mass Spectroscopy (ToF-SIMS) is used to examine low concentrations of foreign elements in the fuel cell anode. ToF-SIMS is capable of part-per-billion (ppb) detection on a surface (2–200 nm depth). It should be noted that absolute quantification of surface concentrations using ToF-SIMS is difficult, so it is normally used to detect trace elements, to compare samples, or to confirm measurement results from other techniques.

An image is generated by rastering a finely focused beam across the sample surface. Due to the parallel detection nature of ToF-SIMS, the entire mass spectrum is acquired from every pixel in the image. The mass spectrum and the secondary ion images are then used to determine the composition and distribution of sample surface constituents.

ToF-SIMS provides spectroscopy for characterization of chemical composition, imaging for determining the distribution of chemical species, and depth profiling for thin film characterization.

Species of interest in the positive ion spectra include; Al, Cd, Cr, Hg, La, Ni, Pb, Sb, Si, Y, Zn, and Zr. The results show that Cd, Hg, Pb, and Zn were not detected or lower than the detection limit (10 ppm). YO₂ and ZrO₂ molecules create an interference with Sb making it difficult to quantify. La is relatively high in Samples 2, 3, 5, 6, 11, and 12, which is qualitatively consistent with XPS results. Cr is also present at low concentrations, but its signal is not strong and is estimated at less than 100 ppm.

Species of interest in the negative ion spectra include; As, C, Ni, P, and S. According to the results, P concentration is relatively high

for Samples 2, 3, 5, 6, 11, and 12 which is also consistent with XPS results. Arsenic is detected at a very low concentration, near the detection limit (10 ppm). However, it is difficult to quantify C and S due to interferences, though their presence is confirmed on the samples.

3.4.3. PIXE

Particle Induced X-ray Emission (PIXE) is an X-ray spectrographic technique, which can be used for the non-destructive, simultaneous elemental analysis of solid samples. In this case, PIXE is used to quantitatively measure the trace elements present in the fuel cell samples. Ion beams do not produce large crystal charging from Bremsstrahlung radiation background effects and the X-ray peaks are well-defined. This contrasts with electron based methods which produce more significant background noise, which diminishes the signal to noise ratio and convolutes peak identification. As such, the detection limits (ppm in most cases) of PIXE are much better than EDX.

The incident beam was 2 MeV with a current of 5 nA. The attenuator was a 160 μm graphite disk charged at 20 μC. PIXE was able to detect Cu, Hf, La, and S as well as some very small quantities of Ca, Cl, and Fe, and the main peaks in the spectrum are identified in Fig. 9. Concentrations obtained from these measurements are shown in Table 6. Similar PIXE spectra are collected from each sample and the concentrations obtained from GUPIX software fitting are also shown in Table 6. Please note that the main elements Ni, Y, and Zr concentrations are not shown in the table. Only trace element concentrations are shown.

3.4.4. TEM

Grain boundary images were collected using a JEOL JEM-2100 Transmission Electron Microscope (TEM). The results show a NiO phase formation between Ni and YSZ particles that increases in size as the applied current density increases. Fig. 10 shows the image taken from cell 11 (maintained at open circuit conditions). There is a clear 8–20 nm formation of NiO at the Ni/YSZ grain boundary (Fig. 10A), while none appears at the Ni/Ni boundary (Fig. 10B). EDS results taken at the point shown in Fig. 10A are given in the corresponding table. Fig. 11 shows the image of taken from cell 10 (operated at 375 mA cm⁻²). There is a much larger 20–80 nm formation of NiO at the Ni/YSZ grain boundary (Fig. 11A), while none appears at the Ni/Ni boundary (Fig. 11B). EDS results taken at the point shown in Fig. 11A are given in the corresponding table. Electron diffraction patterns were also obtained for this area and confirm that the crystal structure is consistent with NiO.

3.4.5. SEM

Images of the cell microstructure were also generated using Scanning Electron Microscopy (SEM). These images did not distinguish appreciable cell structure degradation or structures indicating formation of secondary phases within the anode. This is consistent with results from the other post-trial analysis techniques.

4. Discussion

Of the twelve cells engaged for the test, nine produced statistically relevant data that can be analyzed to examine the processes of contaminant induced degradation. Data collected among the nine cells are used in this section to expand upon the previously offered hypotheses. These hypotheses suggest that degradation occurs from the direct effect of bulk fuel compositions and load conditions. They also suggest degradation due to contaminant specific considerations pertaining to thermo-chemical and thermo-mechanical attack by trace materials and electrochemical operation

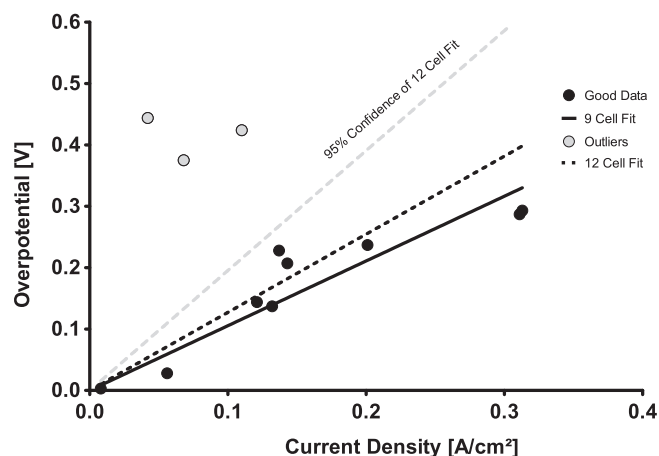


Fig. 4. Cell overpotential as a function of applied current. The outliers correspond to Cells 7, 8, and 12 which are highlighted in Table 3.

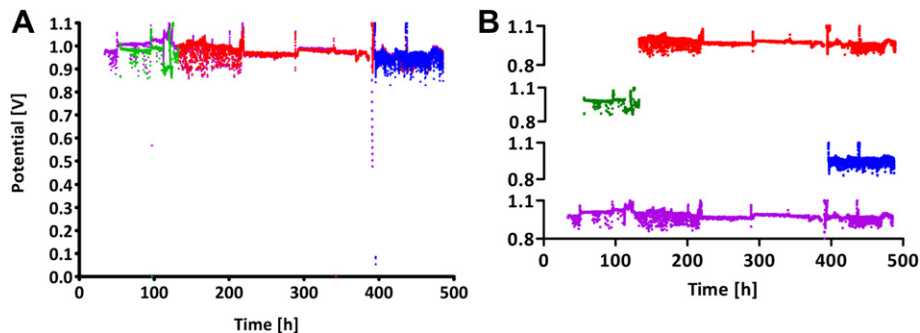


Fig. 5. Plot of potential data for each cell that has held at open circuit potential during the run. In this figure Cell 1 is depicted in red, Cell 4 in green, Cell 5 in blue, and Cell 11 in purple. (For interpretation of the references to colour in this figure legend, the reader is referred to the web version of this article.)

in a contaminant laden fuel. The hypotheses are: 1) Cell degradation occurs due to a degradation of the quality of the supplied fuel; 2) One mode of cell degradation in the presence of direct syngas is purely electrochemical in nature; 3) The presence of syngas contaminants in the direct syngas alone results in cell structure or cell activity degradation; and 4) Exposure of the cell to syngas containing trace contaminants during electrochemical operation accelerates the rate of total cell degradation.

In exploration of hypothesis one, the fuel quality must be compared to the data for cells operated at OCV. The data obtained from cells 1, 4, 5, and 11 indicates that some degradation in potential occurs that is not related to the electrochemical operation of the cells. Analysis reveals a degradation rate of approximately 9% per 1000 h is measured for these cells (Fig. 5 and Table 4). This degradation rate is compared to fuel quality (Nernst potential) over the same period. Fig. 2 indicates that although the quality of the syngas fluctuated over time, when the additional sweetening H_2 is considered in the total syngas flow rate, the syngas quality increases over the duration of the test. Mid-term quality disruptions in the Nernst potential are due to fluctuations in the steam content of the fuel. The average daily syngas Nernst potential is 0.954 ± 0.005 V ($\pm 0.6\%$). The variation in Nernst potential is less than the observed degradation rates of the cells therefore the cell degradation rate does not correspond to a real decrease in fuel quality.

Hypothesis one can therefore be rejected as having a controlling influence on the present test data, and a new hypothesis formulated to explain the observation of decreasing potential in cells held at OCV. If one considers that the cells are driven by the difference in oxygen chemical potential, the decreasing OCV indicates that the difference in oxygen chemical potential is not steadily maintained. New hypotheses should be formed therefore to consider the integrity of components separating bulk oxygen such as the cell

seal and the electrolyte. Whatever the mode of degradation, the degradation rate observed at OCV should be considered as occurring to the same magnitude (on average) in all of the cells and can be subtracted from degradation rates measured for cells operated under load.

Hypothesis two considers whether electrochemically operated cells degrade differently than cells maintained at open circuit potential, and permits evaluation of cell degradation modes that are electrochemical in nature. The relative degradation of cells maintained at OCV and cells operated at some overpotential is obtained by examining data in Figs. 5–8, and the associated degradation rates indicated in Table 4. A non-uniform relationship exists between current density and cell degradation rates, with more rapid degradation measured at higher current density, except at 375 mA cm^{-2} , for which degradation is less than at 250 mA cm^{-2} . More rapid degradation of cells has been frequently reported at higher current density [29,30]. However, the total overpotential of the cells at a given current density in these tests is below typical values expected to result in constituent materials degradation, and relatively low compared to many literature reports.

Cell overpotential as a function of current density can be fit by a linear equation using regression. The coefficient of determination of that fit is 0.828, indicating that 83% of the data are accurately described as a straight line. Therefore, a small portion of the deviation from linearity can be attributed to conditions other than the current density. Referring to Fig. 4, the majority of the squared-error is found in the overpotential of the cells operating at the highest current density. The overpotential is less than the linear function would describe, meaning that these cells performed better than the linear function predicted. This is further explained by the lower overall degradation rate predicted when the cells were operated at 375 mA cm^{-2} (16.2% per 1000 h as opposed to 18.9% at 250 mA cm^{-2}).

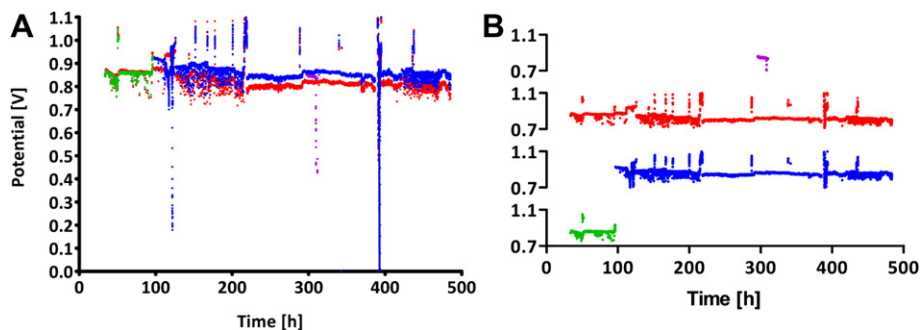


Fig. 6. Plot of potential data for each cell that has held at 125 mA cm^{-2} during the run. In this figure Cell 2 is depicted in purple, Cell 3 in red, Cell 9 in blue, and Cell 10 in green. (For interpretation of the references to colour in this figure legend, the reader is referred to the web version of this article.)

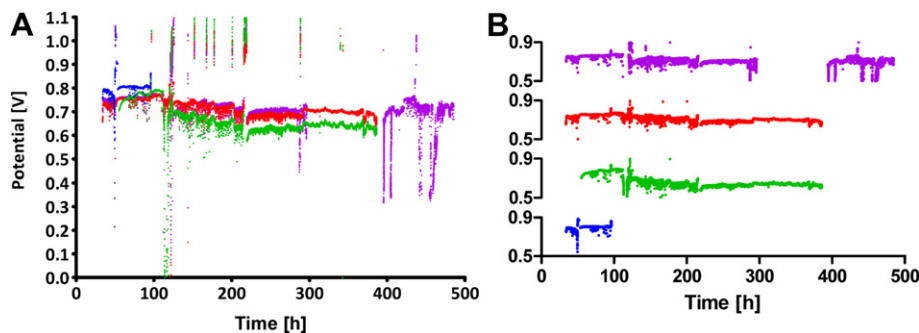


Fig. 7. Plot of potential data for each cell that has held at 250 mA cm^{-2} during the run. In this figure Cell 2 is depicted in purple, Cell 5 in red, Cell 6 in green, and Cell 9 in blue. (For interpretation of the references to colour in this figure legend, the reader is referred to the web version of this article.)

Electrochemical performance could be affected by means other than applied load, and the poor linear correlation of current density to cell degradation supports this idea. Formation of secondary phases or crystallographic changes in key structures of the anode could result in alterations to the electrode conductivity or cell activity. Published literature describes the formation of NiO and *t*-YSZ regions at Ni/YSZ interfaces in the anode [31]. The post-trial crystallographic and nanostructural features of the anode were examined with respect to the formation of secondary phases in intergranular locations or to the collapse of the *c*-YSZ structure to explore this possibility. TEM analysis shows that there is a NiO phase formation in the anode and that the size of the formation increases with increasing current density. Observations made at the electrolyte show a structure that is a combination of *t*-YSZ and *c*-YSZ. The crystallographic phase change of the electrolyte does not seem to correspond to current density differences. Hypothesis two therefore receives support in the observation of NiO intergranular phase growth, which increases with the applied current density. Although the instant of formation of NiO is unknown (it may occur during cooldown for example), phase differences are observed in specimen which differ only with respect to the conditions of electrochemical operation.

Hypothesis three considers degradation modes arising from cell structure or cell activity degradation due to syngas contaminants. Examples include pore filling/blocking due to build-up of carbon, secondary phases formed from the reaction of the cell materials with contaminants, or active site obstruction. The cells were clearly exposed to trace materials and significant quantities of hydrocarbons as shown in Table 2 and Fig. 3, respectively. Among all the known material exposures, some prominent negative actors can be distinguished including C_xH_y , S, P, and As. Data are reviewed separately with consideration given to each element first, and followed by general evaluation of the evidence of thermo-chemical attack.

Carbon may attack the anode via Class I degradation by blocking pores with coke, or via Class III degradation by forming a solid solution of carbon in nickel. At 800°C , carbon is also known to be soluble in nickel at less than 1 atomic percent [32]. There are indications of carbon on the anode surface by ToF-SIMS and XPS (Table 5); however quantification is difficult with these methods. There is no additional conclusive evidence for carbon attack offered by SEM and TEM, though some foreign structures were detected at the Ni/pore interface by TEM. Previously obtained results in lab experiments on naphthalene also imply a thermo-chemical attack route, though similarly scant physical evidence was available and identification of the degradative mode was not possible [33]. In prior tests, the primary evidence of carbon-induced degradation was observation of an increase in the mean Ni grain size. The grain growth was postulated to arise from a process whereby carbon is solubilized in the nickel crystal at high temperature, thereby altering the physical properties of nickel and ultimately facilitating enhanced grain growth. Detailed and meticulous experiments will be necessary to examine this phenomenon, and are reserved for a future effort.

At concentrations less than 2 ppm, sulfur typically deposits on active triple-phase boundary sites, thereby impeding fuel oxidation. Sulfur was present according to ToF-SIMS and PIXE and is known to attack nickel-based SOFC anodes by Class II modes at the concentrations present in these experiments. At the low sulfur exposures observed in these tests, the sulfur will produce a step change decrease in cell voltage that can be subtracted from the total degradation. The performance decrease is typically proportional to current density.

Phosphorus and arsenic will attack nickel in the anode by creating secondary phases (Class III), and published reports indicate that these phases facilitate mobility of Ni that subsequently corrupts the anode microstructure. Phosphorus was detected within the cell and on the cell surfaces by both ToF-SIMS and XPS,

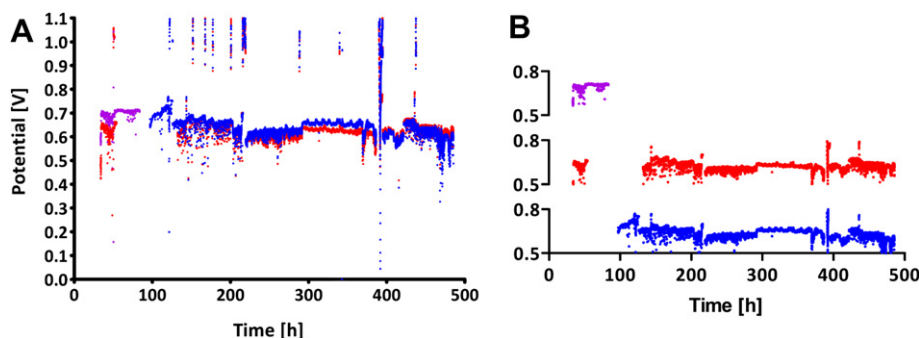


Fig. 8. Plot of potential data for each cell that has held at 375 mA cm^{-2} during the run. In this figure Cell 1 is depicted in purple, Cell 4 in red, and Cell 10 in blue. (For interpretation of the references to colour in this figure legend, the reader is referred to the web version of this article.)

Table 4
Summary of degradation at each current density, including degradation of syngas Nernst potential as determined using a robust linear regression method.

	Nernst potential	Current density [mA cm]			
		0	125	250	375
		mA cm	mA cm	mA cm	mA cm
Degradation [%/1000 h]	None	9.1 ± 0.1%	10.7 ± 0.2%	18.9 ± 0.3%	16.2 ± 0.3%

Table 5
Summary of XPS elemental analysis [weight %].

	C	O	Na	Al	Si	P	Ni	Y	Zr	La
Average	11.5	60.5	1.1	0.7	1.0	0.7	5.2	3.4	16.1	0.5
SD	2.9	2.1	0.3	0.3	0.3	0.6	1.1	0.3	0.9	0.2
Minimum	8.1	56.1	0.4	0.4	0.6	0.2	3.4	2.8	14.2	0.2
Maximum	18.3	62.9	1.6	1.3	1.9	1.8	7.4	3.8	17.5	0.8

and arsenic was identified by ToF-SIMS. Although these elements were detected, no crystalline secondary phases were found in the anode at detectable quantities. SEM/EDS could not locate the characteristic Ni_xP_y structures reported in literature [14,21], and HRTEM could not observe crystallographic distortions or other obvious signs of P and As present in the crystal lattice.

Given that the damage and performance degradations are uniform across all non-outlying cells, contaminant induced modes of degradation remain possible and hypothesis three remains supported. Then returning to the hypothesis, the lack of clear evidence of crystallographic corruption and no evidence of catastrophic microstructural degradation suggests that fuel blockage (Class I) or surface adsorption on the active triple-phase boundary sites (Class II) are the possible route of contaminant caused degradation. Furthermore, considering the degradation observed at OCV, this hypothesis should be expanded to consider seal and electrolyte attack processes as well.

The fourth and final hypothesis considers the effect of exposing the cell to trace materials during polarized operation, and considers whether the degradation rates are accelerated during electrochemical operation. The primary evidence used to examine the hypothesis comes from the SEM and TEM data shown in Figs. 10 and

Table 6
PIXE trace element composition summary [weight %].

	P	S	Cl	Ca	La	Fe	Hf	Cu
Average	0.00	0.73	0.05	0.02	0.16	0.01	1.48	0.24
SD	0.00	0.12	0.04	0.02	0.17	0.02	0.16	0.07
Minimum	0.00	0.57	0.00	0.00	0.00	0.00	1.20	0.17
Maximum	0.00	0.86	0.08	0.04	0.42	0.04	1.60	0.36

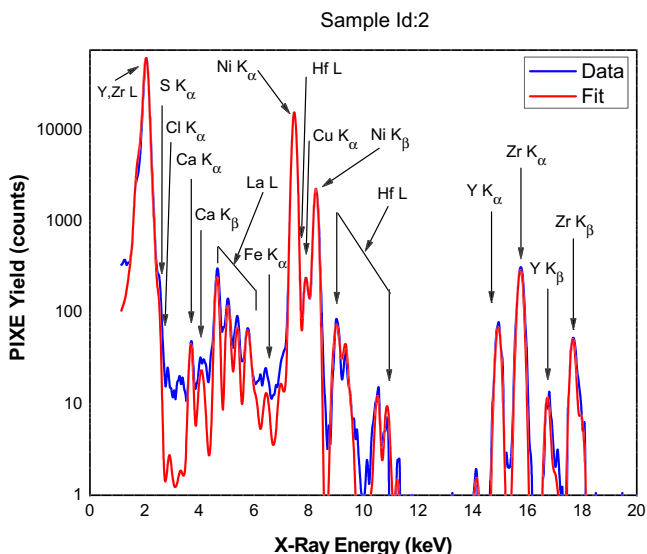
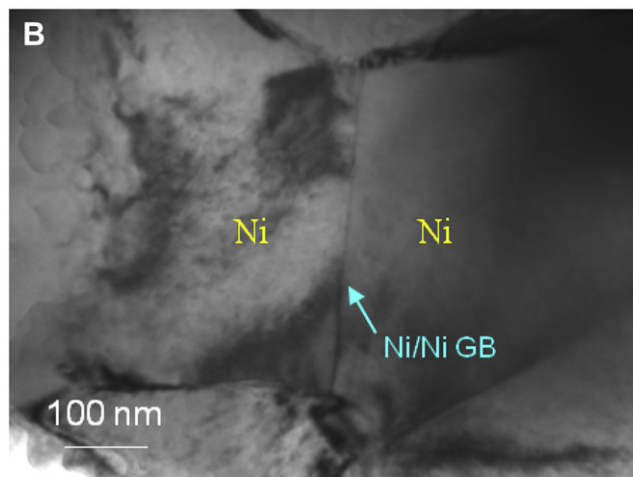
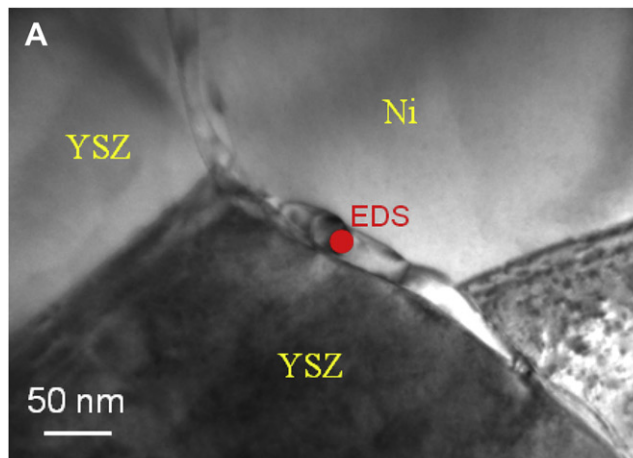
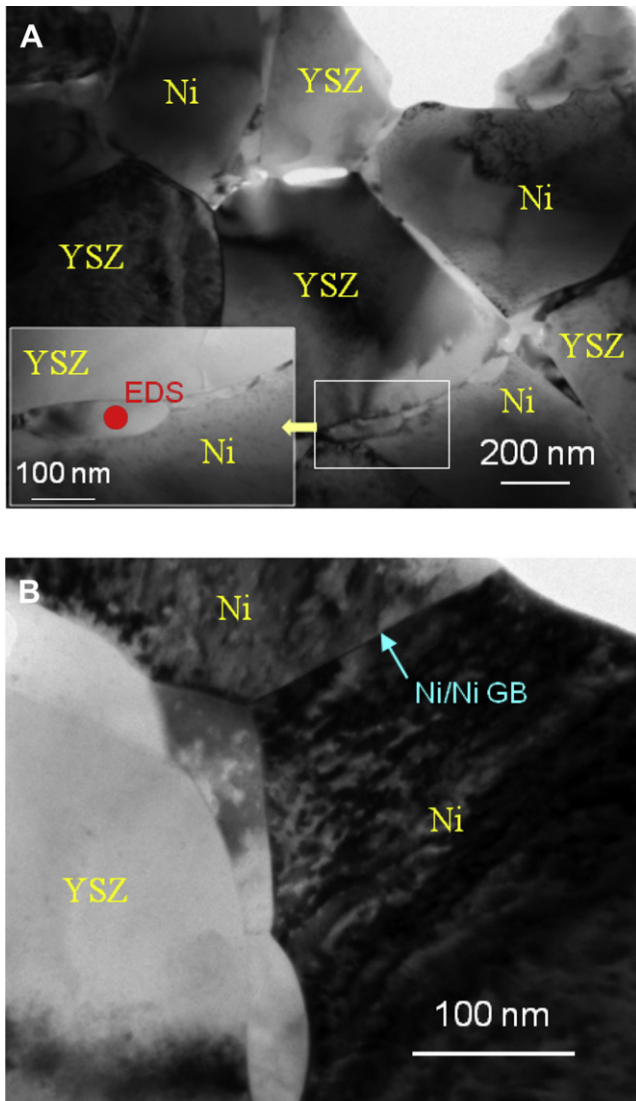


Fig. 9. Representative PIXE results taken from sample #2.

Element	Weight%	Atomic%
O K	10.17	30.63
Ni K	74.78	61.38
Y K	2.46	1.33
Zr K	12.59	6.65
Total	100	100

Fig. 10. TEM image of Cell 11, operated at open circuit conditions. The observed NiO phase varies in size from 8–20 nm.



Element	Weight%	Atomic%
O K	21.31	49.85
Ni K	78.69	50.15
Totals	100.00	100.00

Fig. 11. TEM image of Cell 10, operated at 0.375 mA cm^{-2} . The observed NiO phase varies in size from 20–80 nm.

11. An intergranular phase consisting of NiO is identified in specimen operated at OCV and at 375 mA cm^{-2} , with a larger inclusion observed in the cell operated at higher current density. Although the sample operated at OCV did not undergo polarization in syngas, it was conditioned at 250 mA cm^{-2} for 24 h under hydrogen fuel, and so was polarized for a relatively brief period. The presence of NiO is consistent with previous reports in which intergranular NiO

phases are found in electrochemically operated cells that are cooled in nitrogen [31]. None of the other post-operational analyses detected a statistically significant difference in features among the specimen.

Considering the four hypotheses in total, it appears that degradation potentially arises from four primary modes in the system tested, including: continuous degradation of the cell seal and/or electrolyte; evolution of defects potentially including intrinsic secondary phase formations in anode grain boundaries; relatively small accumulations of incombustible materials in the cell pores and active surfaces; and possible formation of Ni–C solid solutions. Degradation was primarily visible in the structures of the anode and at the grain interfaces, especially in the Ni/YSZ grain boundaries. The evidence also tends to indicate that degradation did not occur by modes including: diminishing fuel quality; direct thermo-chemical attack by phosphorus, arsenic, or other elements; significant coke formation; or electrochemically activated or accelerated processes involving extrinsic materials.

The plausible and rejected modes of degradation are valid for the present test and for any given future combination of test conditions and specimen, any of these modes could be active or inactive and impact the global degradation rate with varying relative significance. For example, phosphorus and arsenic will rapidly degrade cell performance at higher concentration than present here, and Ni_xP_y and Ni_xAs_y formation will be a strong degradation mode.

Finally, the observation of lower degradation at 375 mA cm^{-2} than at 250 mA cm^{-2} must be examined. The two degradation rates are statistically different and unique to the operating current at which they were obtained; therefore experimental uncertainty is not a plausible explanation. It is possible that the principle degradation modes are sensitive through a secondary effect related to current density. An example of this would be degradation modes that are inhibited through an elevated anode water concentration, which would be present at a higher operating current density.

5. Conclusions

The impact on cell operation and performance of fueling SOFC with direct syngas is examined, with the intention to describe the principle modes of degradation expected in an integrated gasification/fuel cell application. Using a specially designed mobile test skid, twelve individual anode-supported SOFC are tested in parallel for over 450 h on direct syngas at the NCCC/PSDF gasification facility in Wilsonville, AL. All twelve cell specimen survived the test, but only nine cells generated reliable data. Cells that were operated at 0 and 125 mA cm^{-2} degraded at 9.1 ± 0.1 and $10.7 \pm 0.2\%$ per 1000 h, respectively, while cells operated at 250 and 375 mA cm^{-2} degraded at 18.9 ± 0.3 and $16.2 \pm 0.3\%$ per 1000 h, respectively. Individual cell performance data and plant data indicating gas composition and trace material exposure are examined in conjunction with post-operational spectroscopic analysis to explain the sources of cell degradation. The analyses imply that primary degradation modes are associated with accumulation of incombustible material in anode pores, formation of Ni–C solid solutions, (intrinsic phase evolution in inter-granular regions), and adsorption of material (such as sulfur) at active sites. Modes of degradation which are not suspected of contributing to degradation in the present test include diminishing fuel quality, direct thermo-chemical attack by phosphorus or arsenic, and coke formation. Although future tests must be completed for the specific conditions in an integrated gasification/fuel cell power generation facility, the results imply that bulk gas conditioning and intrinsic cell stability are of greater concern than elimination of trace contaminant materials.

Acknowledgements

A portion of this research was performed using EMSL, a national scientific user facility sponsored by the Department of Energy's Office of Biological and Environmental Research and located at Pacific Northwest National Laboratory. The authors gratefully acknowledge the NCCC/PSDF facility for hosting the research activity, in particular Tony Wu (Southern Company) and Morgan Mosser (U.S. Department of Energy). The authors also acknowledge the SEM imaging work conducted by James Poston at NETL (U.S. Department of Energy).

References

- [1] K. Gerdes, A. Martinez, R. Gemmen, J. Poston, *Journal of Power Sources* 195 (2010) 5206–5212.
- [2] G.A. Hackett, K. Gerdes, in: U.S.D.o. Energy. (Ed.), *National Energy Technology Laboratory*, Morgantown, WV, 2011.
- [3] J.P. Trembly, R.S. Gemmen, D.J. Bayless, *Journal of Power Sources* 163 (2007) 986–996.
- [4] G.A. Hackett, in: *Department of Chemical Engineering*, West Virginia University, Morgantown, WV, 2009, pp. 122.
- [5] O.A. Marina, L.R. Pederson, D.J. Edwards, C.W. Coyle, J. Templeton, M. Engelhard, Z. Zhu, in: *8th Annual SECA Workshop*, San Antonio, TX, 2007.
- [6] J.P. Trembly, R.S. Gemmen, D.J. Bayless, *Journal of Power Sources* 171 (2007) 818–825.
- [7] J.P. Trembly, R.S. Gemmen, D.J. Bayless, *5th Fuel Cell Science, Engineering, and Technology Conference*, ASME, New York, NY, 2007.
- [8] J. Bao, G.N. Krishnan, P. Jayaweera, K.H. Lau, A. Sanjurjo, *Journal of Power Sources* 193 (2009) 617–624.
- [9] J. Bao, G.N. Krishnan, P. Jayaweera, J. Perez-Mariano, A. Sanjurjo, *Journal of Power Sources* 193 (2009) 607–616.
- [10] J.E. Bao, G.N. Krishnan, P. Jayaweera, A. Sanjurjo, *Journal of Power Sources* 195 (2010) 1316–1324.
- [11] G.N. Krishnan, in: *SRI International*, Morgantown, WV, 2006.
- [12] C.C. Xu, M.Y. Gong, J.W. Zondlo, X.B. Liu, H.O. Finklea, *Journal of Power Sources* 195 (2010) 2149–2158.
- [13] J.P. Trembly, R.S. Gemmen, D.J. Bayless, *Journal of Power Sources* 169 (2007) 347–354.
- [14] C.C. Xu, J.W. Zondlo, H.O. Finklea, O. Demircan, M.Y. Gong, X.B. Liu, *Journal of Power Sources* 193 (2009) 739–746.
- [15] N.Q.Q. Wu, M.J. Zhi, X.Q. Chen, H. Finklea, I. Celik, *Journal of Power Sources* 183 (2008) 485–490.
- [16] O.A. Marina, L.R. Pederson, C.A. Coyle, E.C. Thomsen, P. Nachimuthu, D.J. Edwards, *Journal of Power Sources* 196 (2011) 4911–4922.
- [17] K. Gerdes, J. Trembly, R. Gemmen, *Symposium on Coal Based Fuel Cell Technology*, National Institute of Fuel Cell Technology, Morgantown, WV, 2007.
- [18] Y. Matsuzaki, I. Yasuda, *Solid State Ionics* 132 (2000) 261–269.
- [19] S. Mukerjee, K. Haltiner, R. Kerr, L. Chick, V. Sprenkle, K. Meinhardt, C. Lu, J.Y. Kim, K.S. Weil, *ECS Transactions* 7 (2007) 59–65.
- [20] K. Sasaki, K. Susuki, A. Iyoshi, M. Uchimura, N. Imamura, H. Kusaba, Y. Teraoka, H. Fuchino, K. Tsujimoto, Y. Uchida, N. Jingo, *Journal of the Electrochemical Society* 153 (2006) A2023–A2029.
- [21] O.A. Marina, C.A. Coyle, E.C. Thomsen, D.J. Edwards, G.W. Coffey, L.R. Pederson, *Solid State Ionics* 181 (2010) 430–440.
- [22] L.R. Pederson, C.A. Coyle, O.A. Marina, E.C. Thomsen, D.J. Edwards, C.D. Cramer, G.W. Coffey, *Journal of Power Sources* 193 (2009) 730–738.
- [23] X. Guan, B. Gardner, R.A. Martin, J. Spain, *Powder Technology* 180 (2008) 122–128.
- [24] F. Wallace, X. Guan, R. Leonard, M. Nelson, P. Vimalchand, W.W. Peng, P.V. Smith, R.W. Breault, in: *Thirty-First International Technical Conference on Coal Utilization and Fuel Systems*, Clearwater, FL, USA, 2006.
- [25] H.J. Motulsky, R.E. Brown, *BMC Bioinformatics* 7 (2006) 123.
- [26] K. Park, S. Yu, J. Bae, H. Kim, Y. Ko, *International Journal of Hydrogen Energy* 35 (2010) 8670–8677.
- [27] L.K. Chiang, H.C. Liu, Y.H. Shiu, C.H. Lee, R.Y. Lee, *Renewable Energy* 33 (2008) 2580–2588.
- [28] S.D. Vora, *12th Annual SECA Workshop*, SECA, Pittsburgh, PA, 2011.
- [29] A. Hagen, R. Barfod, P.V. Hendriksen, Y.-L. Liu, S. Ramousse, *Journal of the Electrochemical Society* 153 (2006) A1165–A1171.
- [30] A. Hagen, P.V. Hendriksen, H.L. Frandsen, K. Thyden, R. Barfod, *Fuel Cells* 9 (2009) 814–822.
- [31] Y. Chen, S. Chen, G.A. Hackett, H. Finklea, X. Song, K. Gerdes, *Solid State Ionics* (2011).
- [32] D. Laplaze, L. Alvarez, T. Guillard, J.L. Sauvajol, G. Flamant, *Chemical Physics Letters* 342 (2001) 7–14.
- [33] K. Gerdes, in: *11th Annual SECA Workshop*, Pittsburgh, PA, 2010.